Mechanically-Activated Synthesis and Mixed Conductivity of TbMO$_{4-\delta}$ (M = Zr, Hf) Ceramics

E.V. TSIPIS,[1] A.V. SHLYAKHTINA,[2] L.G. SHCHERBAKOVA,[2] I.V. KOLBANEV,[2] V.V. KHARTON,[1,3,*]
N.P. VYSHATKO[1] & J.R. FRADE[1]

[1]*Department of Ceramics and Glass Engineering, CICECO, University of Aveiro, 3810-193 Aveiro, Portugal*
[2]*Semenov Institute of Chemical Physics, Russian Academy of Sciences, 4 Kozigina Str., 119991 Moscow, Russia*
[3]*Institute of Physicochemical Problems, Belarus State University, 14 Leningradskaya Str., 220050 Minsk, Belarus*

Abstract. Terbium hafnate and zirconate ceramics with submicron grain sizes were prepared via mechanically-activated synthesis. X-ray and electron diffraction and infrared (IR) absorption spectroscopy showed that TbZrO$_{4-\delta}$ has a disordered fluorite-type structure, while TbHfO$_{4-\delta}$ is partially ordered, containing pyrochlore microdomains. The oxygen ion transference numbers determined by the modified e.m.f. technique under oxygen/air gradient, vary in the range 0.08–0.26 at 873–1123 K, increasing with temperature. The activation energies for ionic and *p*-type electronic transport are 82–83 and 29–40 kJ/mol, respectively. The ionic conduction becomes dominant in reducing atmospheres, but tends to decrease at low *p*(O$_2$). Oxygen partial pressure dependencies of Seebeck coefficient can be described by a model common for oxide phases with mixed ionic and electron-hole conductivity. Due to partial cation ordering, terbium hafnate exhibits lower ionic and hole transport as compared to TbZrO$_{4-\delta}$. The average thermal expansion coefficients of TbMO$_{4-\delta}$ (M = Zr, Hf) ceramics in air, calculated from dilatometric data, are (11.5–12.4) × 10^{-6} K^{-1} at 600–1200 K and (18.4–20.3) × 10^{-6} K^{-1} at 1200–1420 K.

Keywords: terbium zirconate, terbium hafnate, fluorite, mechanical activation, mixed conductor

Introduction

Numerous oxide materials with pyrochlore- and fluorite-type crystal lattices possess a significant oxygen ionic conductivity and thus are of interest for high-temperature electrochemical applications, including solid oxide fuel cells (SOFCs), gas separation membranes and sensors [1–7]. For this group of solid electrolytes, the highest ionic transport is observed for Bi$_2$O$_3^-$, CeO$_2$- and ZrO$_2$-based fluorite materials [5–7]. However, a substantially high level of ionic conduction is also characteristic of some pyrochlores, such as Gd$_2$Zr$_2$O$_7$ or Ca-doped Gd$_2$Ti$_2$O$_7$ [1–4]. The lattice of A$_2$B$_2$O$_7$ pyrochlore can be considered as a superstructure based on fluorite (A,B)O$_2$, where the cations and anion vacancies are both ordered [8, 9]. The pyrochlore structure contains one vacant oxygen site per formula unit, which would be occupied in case of fluorite; these unoccupied sites may provide pathways for fast oxygen transport [8, 9].

At elevated temperatures, typically around 1650–2500 K, most pyrochlores disorder into fluorite polymorphs [3, 9]. Decreasing A-site cation radius increases stability of fluorite modifications, thus favoring "pyrochlore → fluorite" transition [3, 4, 7–9]. When induced by such cation composition variations, this transformation is rather gradual and occurs via partial ordering of various types [3, 10]. In particular, for Tb$_2$Zr$_2$O$_7$ where the A/B cation radius ratio is close to the "pyrochlore-fluorite" boundary, X-ray diffraction (XRD) analysis suggests a fluorite structure [3, 4],

*To whom all correspondence should be addressed. E-mail: kharton@cv.ua.pt

while the transmission electron microscopy (TEM) indicates short-range order phenomena [3]. Analogously, $Tb_2Hf_2O_7$ can be obtained in both polymorph modifications, depending on synthesis method and processing conditions [7, 11, 12].

One should note that the incorporation of variable-valence cations into either pyrochlore or fluorite structure results, as a rule, in a higher electronic conductivity. This may be of interest for applications in oxygen separation membranes and SOFC electrodes, where both ionic and electronic transport should be as high as possible. $Tb_2Zr_2O_{7+\delta}$ is known as a mixed conductor with oxygen ion transference numbers (t_o), varying from approximately 0.08 to 0.40 at 973–1173 K in air [4]. Electronic transport, which occurs due to hopping of p-type charge carriers between terbium cations via a small-polaron mechanism, decreases with decreasing oxygen partial pressure; the ionic conduction becomes dominant in reducing atmospheres [4]. At the same time, comparison of the ionic conductivity values, extracted from the total conductivity at $p(O_2)$ lower than 10^{-15} atm and determined using an oxygen concentration cell, shows significant disagreements at temperatures below 1023 K [4].

The present work is focused on the study of transport properties of $TbZrO_{4-\delta}$ and $TbHfO_{4-\delta}$ ceramics with submicron grain size, prepared via mechanically-activated synthesis. As for other synthesis methods resulting in nano- and submicron-scale crystallites, such as cryochemical and sol-gel techniques, the use of mechanochemical activation often leads to enhanced defect concentrations, formation of metastable disordered phases and, subsequently, to considerable variations in the ionic and electronic transport properties (for instance [7, 13, 14] and references therein). Theoretical prediction of such changes is difficult due to the complex nature of transport processes occurring at grain boundaries and in nanosized grains. The development of novel materials for electrochemical applications requires, therefore, empirical knowledge of the role of the processing route. Since $TbZrO_{4-\delta}$ and $TbHfO_{4-\delta}$ both possess A/B cation radius ratio close to the "pyrochlore-fluorite" boundary in the systems $Ln_2M_2O_{7+\delta}$ (M = Zr, Hf; Ln is rare-earth cation), mechanically-activated synthesis may have a strong effect on the structure and phase composition. Particular emphasis in this work is therefore given to the structural characterization of terbium zirconate and hafnate ceramics.

Experimental

Single-phase $TbZrO_{4-\delta}$ and $TbHfO_{4-\delta}$ were synthesized from mechanically activated mixtures of stoichiometric amounts of high-purity terbium, zirconium and hafnium oxides. The mechanical activation was performed in a high-energy eccentric-type vibration mill (1200 rpm, 10 h, air atmosphere, batch of 20 g, mixture/balls weight ratio of 0.5–0.7), according to Ref. [15]. After milling, powders were pressed into discs (diameter 10 mm, 300 kg/cm^2), placed into a furnace preheated to 523 K, and then fired in air at 1473 K for 6 h with subsequent slow cooling. This procedure was selected on the basis of experimental data on phase development in the activated mixtures, partly discussed below. In the course of optimization of processing conditions, XRD studies were carried out on a DRON-3M diffractometer (CuK$_\alpha$ radiation); final XRD patterns used for the Rietveld refinement were collected using powders, obtained by grinding of the ceramic samples, using a Rigaku D/Max-B instrument (CuK$_\alpha$, $2\theta = 10$–$100°$, step $0.02°$, 6 s/step). Fullprof software [16] was used for the structure refinement. Infrared (IR) absorption spectra were recorded at room temperature in the frequency range 250–4000 cm^{-1}, using the KBr pellet technique and a SPECORD M-80 instrument. Ceramic microstructure was characterized by scanning and transmission electron microscopy (SEM and TEM) coupled with energy dispersive spectroscopy (EDS); Hitachi S-4100 and H-9000 microscopes were used for SEM and TEM, respectively. Dilatometric data (heating/cooling rate of 5 K/min) were obtained using a BAHR Thermoanalyse DIL801L apparatus, in air.

The description of equipment and experimental procedures used for electrical characterization, including the measurements of total conductivity, Seebeck coefficient and transference numbers, was published elsewhere ([17–22] and references therein). In order to avoid time degradation of the electrical properties observed at 1223 K caused by microstructural changes, the temperature range for all measurements was limited to 1123 K. Total conductivity (σ) was determined using AC impedance spectroscopy data (Hewlett Packard 4284 A Precision LCR Meter, frequency range 20 Hz–1 MHz) collected in flowing air, argon, and 10%H$_2$-90%N$_2$ mixture at 373–1123 K. The Seebeck coefficient (α) was studied in the temperature range 1023–1123 K as a function of the oxygen partial pressure, $p(O_2)$, varying in the range from 10^{-24} to 0.36 atm; the measurement technique was described earlier [17, 18].

The oxygen ion transference numbers (t_o) were determined at 873–1123 K by the modified e.m.f. technique, taking electrode polarization into account [19–21]; most measurements were performed under oxygen/air gradient. The values of partial ionic (σ_o) and p-type electronic (σ_p) conductivities were calculated from the data on total conductivity and transference numbers as $\sigma_o = t_o \times \sigma$ and $\sigma_p = (1 - t_o) \times \sigma$, respectively.

Fig. 2. XRD patterns of TbZrO$_{4-\delta}$ after mechanical activation and after firing at 1473 K.

Results and Discussion

Phase Development

Room-temperature XRD data illustrating phase changes in the mixture of terbium and hafnium oxides after mechanical activation are presented in Fig. 1. The as-treated mixture contains a significant amorphous fraction, which disappears on heating; the formation of single-phase TbHfO$_{4-\delta}$ is completed only after annealing at 1473 K for 6 h. On the contrary, the initial terbia-hafnia mixture fired in identical conditions without mechanical activation still contains large amounts of the starting materials, comparable to the amount of TbHfO$_{4-\delta}$. The mechanically-activated synthesis route hence 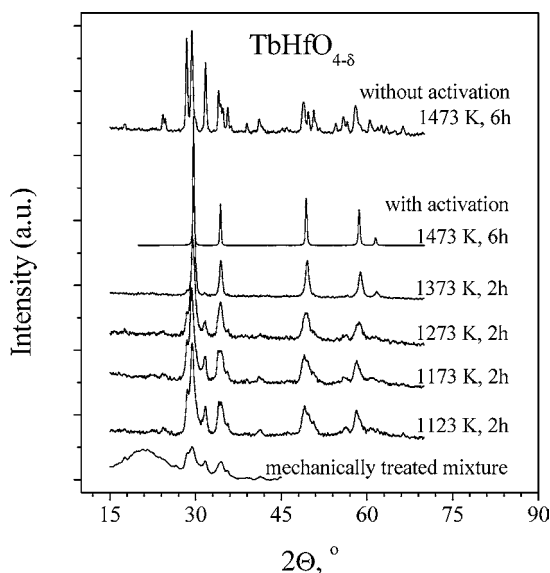makes it possible to decrease the temperature and time necessary for the solid-state reaction, as expected. The behavior of terbia-zirconia mixtures was found similar; a single fluorite-like phase of TbZrO$_{4-\delta}$ was formed after firing at 1473 K for 6 h. In this case, the XRD patterns (Fig. 2) might suggest that the formation of the final product started even in the course of mechanical treatment; however, conclusion regarding to possible mechanically-induced synthesis is ambiguous due to peak broadening and presence of the amorphous phase. XRD analysis repeated after aging of the ceramic samples at 1123 K for 100 h, showed no changes in the phase composition or lattice parameter.

Structure and Microstructure

The final Rietveld plots of TbHfO$_{4-\delta}$ and TbZrO$_{4-\delta}$ are given in Fig. 3. For both compositions, Rietveld refinement was performed presuming two possible crystal structures, namely pyrochlore Tb$_2$M$_2$O$_{7+\delta}$ (space group Fd$\bar{3}$m, No.227) and fluorite TbMO$_{4-\delta}$ (S.G. Fm$\bar{3}$m, No.225). The pyrochlore lattice is distinguished from fluorite by ordering of the cations in 16d (1/2,1/2,1/2) and 16c (0,0,0) sites, and by the displacement of 48f oxygen. In XRD patterns this should be reflected by additional Bragg peaks, particularly (311) (for CuK$_\alpha$ radiation 2θ $\approx$ 28.5°) and (331) (2$\theta \approx$ 37.5°). These lines are not observed in the XRD spectra (Fig. 3). Therefore, if considering XRD data only, the structure of both studied compounds should be described as cubic fluorite; Table 1 lists the unit cell parameters and agreement factors for the Fm$\bar{3}$m space group. The lattice parameters of TbHfO$_{4-\delta}$ and TbZrO$_{4-\delta}$ are very similar, as a result of the similar radii of Zr^{4+} and Hf^{4+} cations [22].

Fig. 1. XRD patterns showing phase development in the stoichiometric terbia-hafnia mixture with and without preliminary mechanical activation.
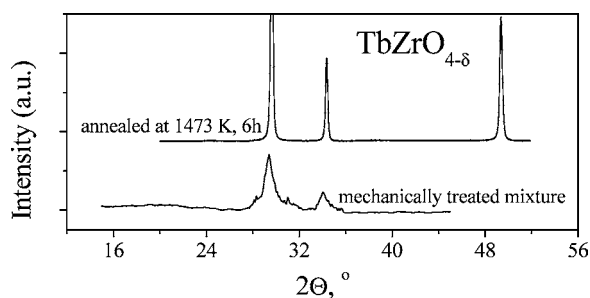
Table 1. Properties of TbHfO$_{4-\delta}$ and TbZrO$_{4-\delta}$ ceramics

Composition	Unit cell parameter		Grain size (nm)	Average thermal expansion coefficient		Activation energy for the total conductivity	
	S.G.	a, Å		T (K)	$\bar{\alpha} \times 10^6$ (K^{-1})	T (K)	E_a (kJ/mol)
TbHfO$_{4-\delta}$	Fm$\bar{3}$m	5.222(9)	50–150	600–1200	11.53 ± 0.01	873–1123	44 ± 1
				1200–1420	18.37 ± 0.08	423–723	57 ± 2
TbZrO$_{4-\delta}$	Fm$\bar{3}$m	5.221(1)	70–200	600–1200	12.36 ± 0.02	773–1123	36 ± 1
				1200–1420	20.28 ± 0.07	373–723	49 ± 1

Notes: R$_p$, P$_{wp}$ and χ^2 factors are equal to 7.15, 8.59 and 5.32 for Tb$_2$Hf$_2$O$_{7+\delta}$, and 7.56, 6.82 and 2.68 for TbZrO$_{4-\delta}$, respectively; the activation energy values are calculated by standard Arrhenius model, $\sigma T = A_0 \times \exp(-E_a/RT)$.
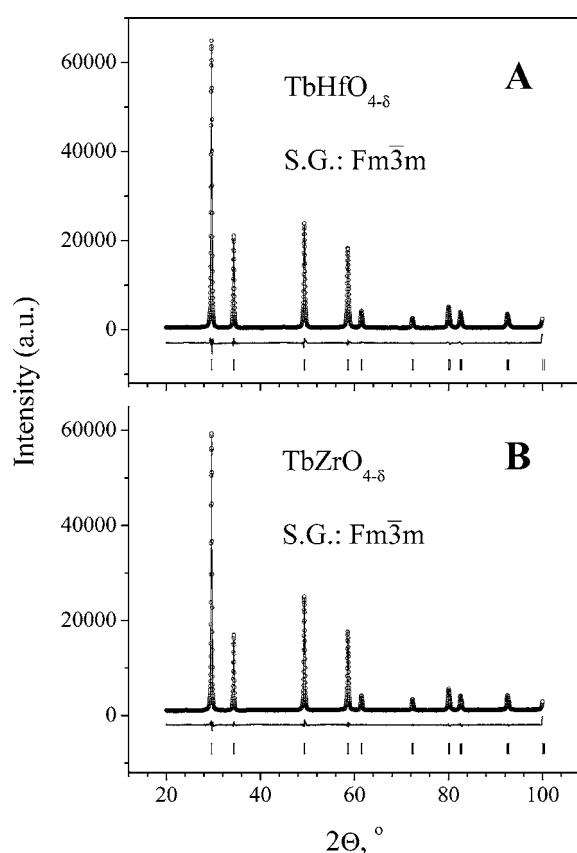

Fig. 3. Observed, calculated and difference XRD patterns of TbHfO$_{4-\delta}$ (A) and TbZrO$_{4-\delta}$ (B).

One should separately note that the XRD results cannot exclude local ordering [3, 10, 23]. Moreover, in the case of TbHfO$_{4-\delta}$, the intensity of (311) and (331) Bragg peaks is expected to be very low due to only

a small difference in the atomic scattering factors of hafnium and terbium; these reflections could hence be missed. As an attempt to reveal possible local ordering, selected area electron diffraction (SAED) and IR absorption studies were performed.

Representative examples of the SAED patterns of TbHfO$_{4-\delta}$ and TbZrO$_{4-\delta}$ are presented in Fig. 4 (A) and (B). All observed reflections are consistent with fluorite structure; no superlattice spots or diffuse scattering characteristic of locally-ordered (Tb,Gd)$_2$Zr$_2$O$_7$ [23] can be seen in the electron diffraction patterns in both cases. At the same time, the IR spectrum of TbHfO$_{4-\delta}$ exhibits absorption bands at 400 and 510 cm^{-1} (Fig. 5), typical for Ln$_2$Hf$_2$O$_7$ pyrochlore structure [24]. Such behavior indicates a partial pyrochlore-type ordering in terbium hafnate ceramics. The fact, that ordered microdomains cannot be distinguished in the course of standard TEM analysis, may be explained if their volume fraction is small and/or if their primary location is around grain boundaries. Also, one should take into account the very similar values of the atomic scattering factors of Hf and Tb, which should lead to weakening of possible superlattice reflections. In these conditions, detailed HRTEM studies are necessary to resolve microdomain formation.

For TbZrO$_{4-\delta}$, no absorption band near 510 cm^{-1} is observed in the IR spectra (Fig. 5), in agreement with X-ray and electron diffraction data. Therefore, the structure of terbium zirconate can be identified as disordered fluorite-type. This may be considered as contradicting to the data of van Dijk et al. [3, 23] who reported a short-range ordering in TbZrO$_{4-\delta}$ ceramics with micron-scale grain size, prepared using citrate method and sintered at 1823 K. Such a difference results, most probably, from the microstructural features of
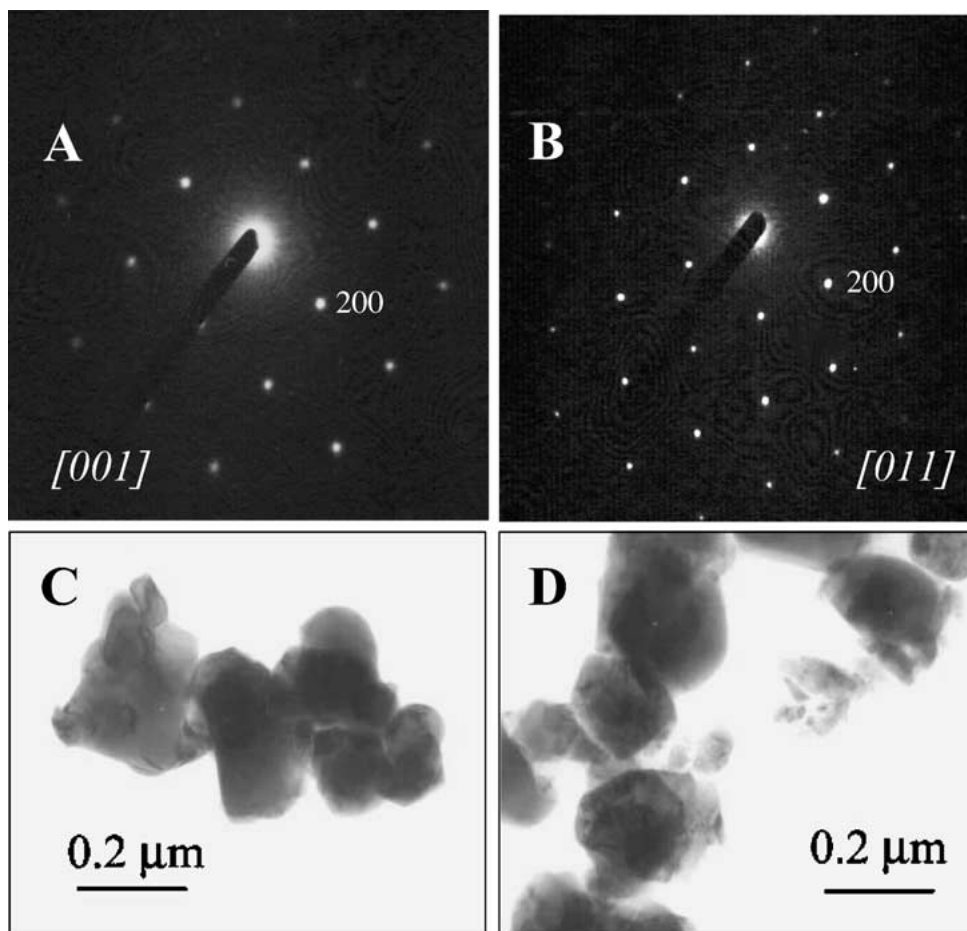
Fig. 4. Selected area electron diffraction patterns of TbHfO$_{4-\delta}$ along [001] zone axis (A), and TbZrO$_{4-\delta}$ along [011] zone axis (B), and the bright-field TEM images of TbHfO$_{4-\delta}$ (C) and TbZrO$_{4-\delta}$ (D). SAED patterns can be indexed for the cubic fluorite cell.

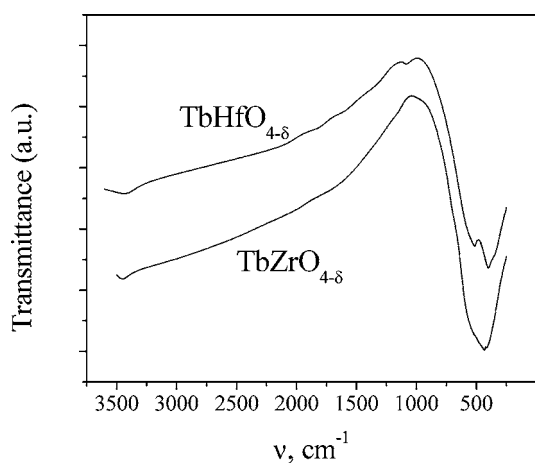*Fig. 5*. IR absorption spectra of TbZrO$_{4-\delta}$ and TbHfO$_{4-\delta}$.

terbium zirconate obtained via mechanically-activated synthesis, where the grains are considerably smaller and a greater concentration of extended defects, such as dislocations, may be expected. In addition, the sintering conditions used in the present work were quite different from those reported by van Dijk et al. [3, 23]. For instance, due to the strong effect of submicron grain size on the properties of ceramic materials, the use of sol-gel or organometallic-precursor techniques often leads to apparent stabilization of cubic fluorite Zr(Ln)O$_{2-\delta}$ phases, the composition of which corresponds to multiphase domains in equilibrium phase diagrams, at temperatures below 1300–1350 K [7]. Another necessary comment is that the different behavior of TbHfO$_{4-\delta}$ and TbZrO$_{4-\delta}$ is in agreement with literature data [6, 7] showing a higher
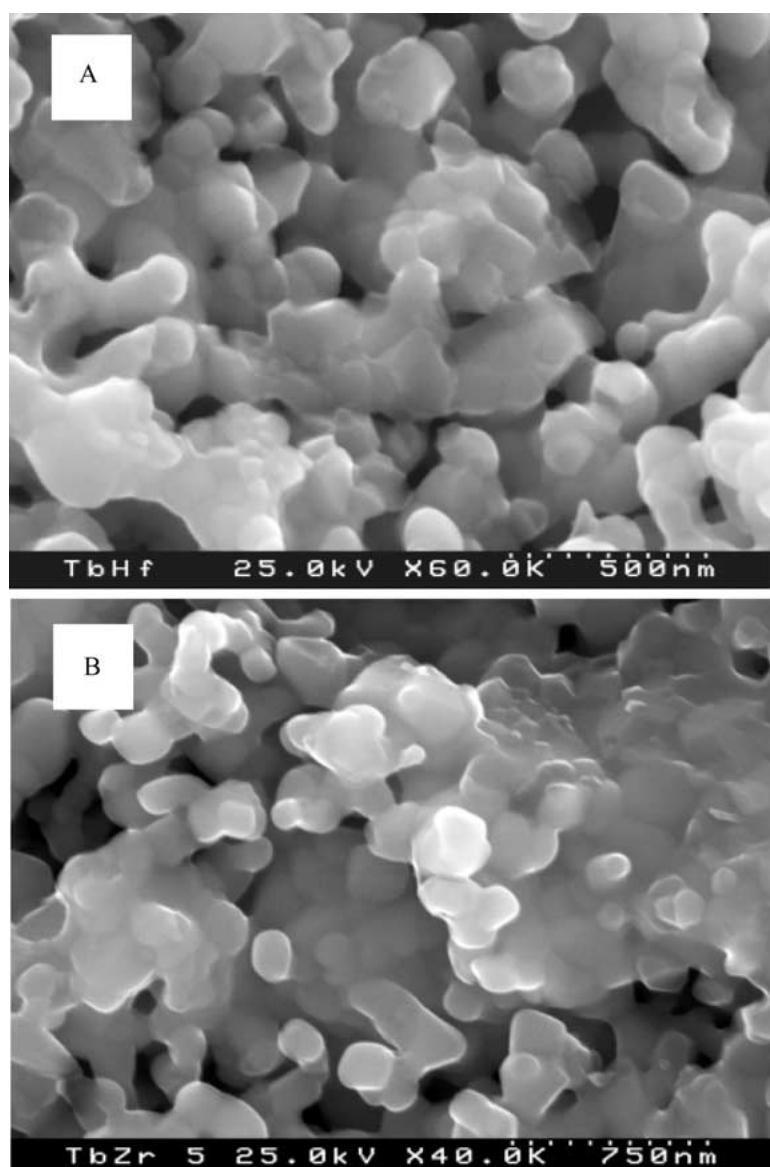
Fig. 6. SEM micrographs of fractured ceramic samples: TbHfO$_{4-\delta}$ (A) and TbZrO$_{4-\delta}$ (B).

thermodynamic stability of HfO$_2$-containing py-rochlores with respect to ZrO$_2$-based compounds, while the stabilized fluorite phases in HfO$_2$- and ZrO$_2$-based systems show the opposite tendency.

Typical SEM micrographs of fractured TbMO$_{4-\delta}$ samples are shown in Figs. 6 and 4(C) and (D) present two examples of bright-field TEM images. The grain size distribution in both materials is quite uniform; no inhomogeneities in the cation distribution between grains and grain boundaries were detected by EDS analysis. The grain size, which is slightly smaller for terbium hafnate ceramics, varies from 50 to 200 nm. The low limit of this range, 50 nm, is close to crystallite size estimates from the XRD data, 46.4–50.2 nm. In addition, TEM studies indicated no traces of liquid phase or other grain-boundary phenomena, in agreement with the impedance spectroscopy data discussed below.
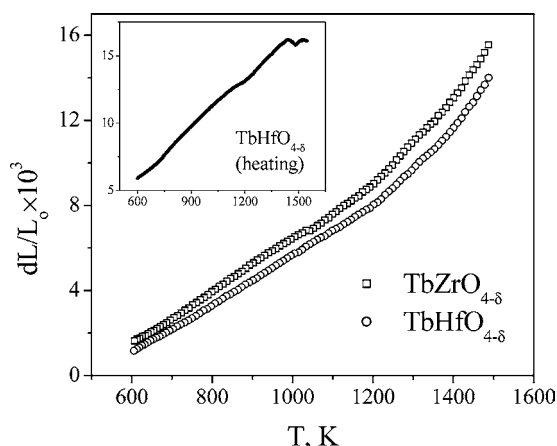
Fig. 7. Dilatometric curves of TbZrO$_{4-\delta}$ and TbHfO$_{4-\delta}$ ceramics on cooling in air. Inset shows the curve of TbHfO$_{4-\delta}$ on heating up to 1600 K, illustrating the shrinkage behavior.
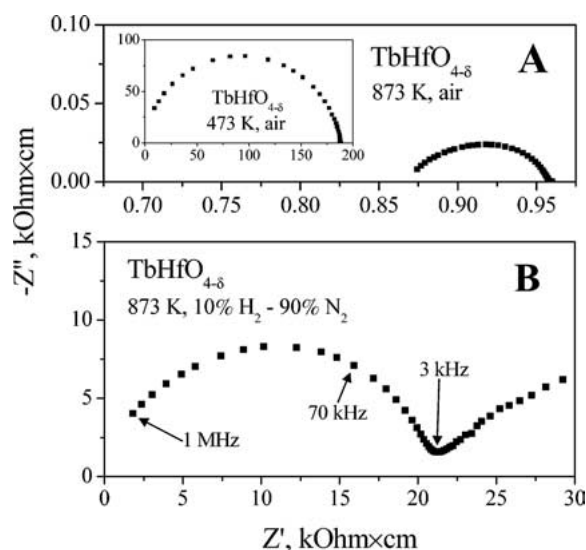

Fig. 8. Impedance spectra of TbHfO$_{4-\delta}$ ceramics in air (A) and in a flow of 10%H$_2$–90%N$_2$ mixture (B).
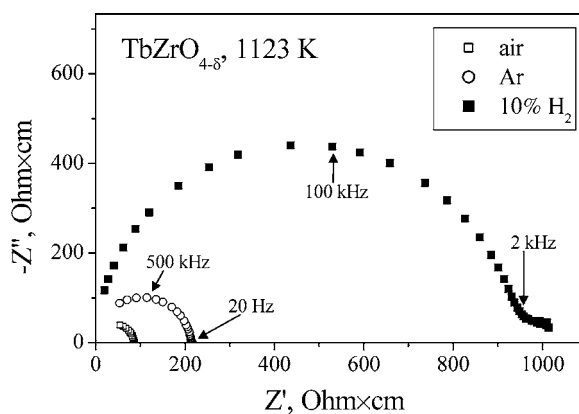
Fig. 9. Impedance spectra of TbZrO$_{4-\delta}$ ceramics in various atmospheres at 1123 K.

Thermal Expansion

Dilatometric studies of TbMO$_{4-\delta}$ ceramics showed that heating up to temperatures, comparable to the temperature of final firing, leads to continuing shrinkage processes. One example illustrating such behavior is presented as inset in Fig. 7. The shrinkage starts at 1440–1460 K for TbHfO$_{4-\delta}$ and 1470–1490 K for TbZrO$_{4-\delta}$. This suggests that, although the conductivity degradation is observed at 1223 K, grain growth becomes extensive at significantly higher temperatures. In the intermediate temperature range, 1200–1400 K, the dilatometric curves of TbMO$_{4-\delta}$ show a considerable nonlinearity, probably associated with starting microstructural changes and oxygen losses from the lattice on heating (Fig. 7). At lower temperatures, the dilatometric curves are approximately linear, with the average thermal expansion coefficients (TECs) of $(11.5–12.5) \times 10^{-6}$ K^{-1} (Table 1). These values are close to literature data on (Gd,Ca)$_2$Ti$_2$O$_7$ [25], Y$_2$(Ti,Zr)$_2$O$_7$ [9] and Ln$_2$Hf$_2$O$_7$ [6] pyrochlores, being slightly higher than TECs of stabilized zirconia ceramics [7].

Ionic and p-Type Electronic Conductivity in Oxidizing Conditions

Typical impedance spectra of TbHfO$_{4-\delta}$ and TbZrO$_{4-\delta}$ ceramics are presented in Figs. 8 and 9, correspond-

ingly. In all cases, no grain-boundary contribution was detected even at low temperatures (for example, inset in Fig. 8(A)). The spectra collected in air consist of a bulk arc and a small electrode tail, the latter decreasing with reducing temperature. Such a behavior indicates that the p-type electronic contribution to the total conductivity is dominant in oxidizing atmospheres and possesses an activation energy lower than that for ionic conduction. Indeed, the oxygen ion transference numbers measured by the modified e.m.f. method under oxygen/air gradient, vary in the range

Table 2. Parameters of oxygen ion transport

Composition	Ion transference number under oxygen/air gradient		Activation energy for ionic and electronic conductivities, kJ/mol	
	T, K	t_o	$E_a (\sigma_o)$	$E_a (\sigma_p)$
TbHfO$_{4-\delta}$	1123	0.26	82 ± 7	40 ± 2
(873–1123) K	1073	0.21		
	1023	0.17		
	973	0.14		
	923	0.11		
	873	0.09		
TbZrO$_{4-\delta}$	1123	0.25	83 ± 9	29 ± 2
(923–1123) K	1073	0.20		
	1023	0.14		
	973	0.12		
	923	0.08		

Fig. 10. Temperature dependence of oxygen ionic and *p*-type electronic conductivity of TbMO$_{4-\delta}$ ceramics in air. Inset shows temperature dependence of the total conductivity.

0.08–0.26 at 873–1123 K and increase with temperature (Table 2). A qualitatively similar trend, namely a higher activation energy (E_a) for the ionic transport compared to *p*-type electronic, is characteristic of a number of fluorite- and pyrochlore-type phases containing variable-valence cations [1, 6, 7, 25]. The values of E_a for ionic conduction, 82–83 kJ/mol at 873–1123 K in air (Table 2), are also consistent with literature data on pyrochlore zirconates and fluorite-type solid solutions based on stabilized zirconia [3, 4, 6–9]. For instance, these values were reported to vary in the range 67–116 kJ/mol for Ln$_2$Zr$_2$O$_7$ (Ln = Nd, Sm, Gd, Tb, Er) [3] and 84 kJ/mol for Nd$_2$Hf$_2$O$_7$ [6]; typical E_a range for stabilized cubic ZrO$_2$ correspond to approximately 62–84 kJ/mol [7]. The activation energies for *p*-type electronic conductivity, 29–40 kJ/mol (Table 2), are slightly higher than expected for a small-polaron mechanism. Most probably, this may be attributed to the oxygen losses on heating [4], decreasing hole concentration and, thus, influencing apparent activation energy for the hole transport.

Due to the partial cation ordering in TbHfO$_{4-\delta}$, the partial ionic and *p*-type electronic conductivities of terbium hafnate are both lower than those of TbZrO$_{4-\delta}$ (Fig. 10). Again, this is in an excellent agreement with literature data [6, 7], showing that the pyrochlorefluorite transition is accompanied with increasing ionic conduction, and that the transport properties of HfO$_2$-based materials are usually worse compared to ZrO$_2$-based ceramics. The latter results from a greater tendency to local ordering in hafnates [6]. Respectively,
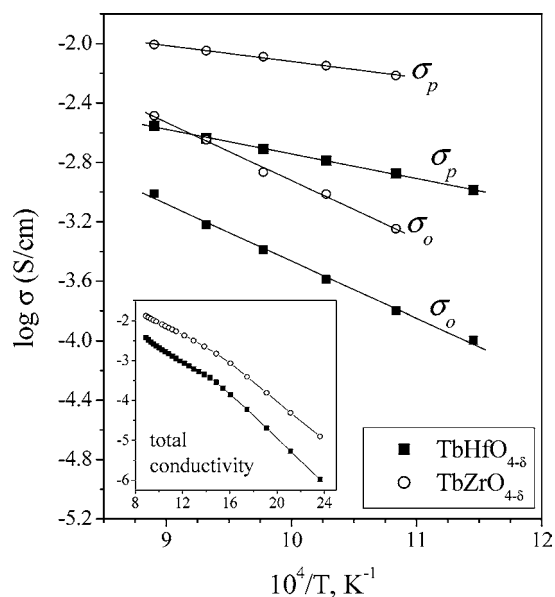
at 673-1123 K the total conductivity of TbZrO$_{4-\delta}$ is 3–5 times higher than that of TbHfO$_{4-\delta}$, whereas the activation energy values are similar for both materials (inset in Fig. 10). Notice that changes in the slope of the Arrhenius curves at 600–700 K are related to oxygen losses on heating, which leads to decreasing *p*-type charge carrier concentration [4].

Finally, Fig. 11 compares the transport properties of TbZrO$_{4-\delta}$ ceramics with submicron grain size, prepared in this work, with data on the same material where the grains were 10–20 times larger [4]. In the latter case, both ionic and electron-hole conductivities are slightly higher. Such a difference might seem quite surprising as the IR and SAED studies of TbZrO$_{4-\delta}$, prepared via mechanical activation, showed no local ordering and the impedance spectroscopy indicated that the grain-boundary resistance is insignificant (Fig. 9). On the contrary, SAED patterns of terbium zirconate studied by van Dijk et al. [3, 23] clearly demonstrate short-range ordering phenomena; a considerable grain-boundary contribution is also observed in the impedance spectra [4]. The observed behavior could be explained by a greater concentration of extended linear defects (e.g. dislocations) trapping charge carriers in the ceramics prepared using mechanically-activated synthesis. Note that the
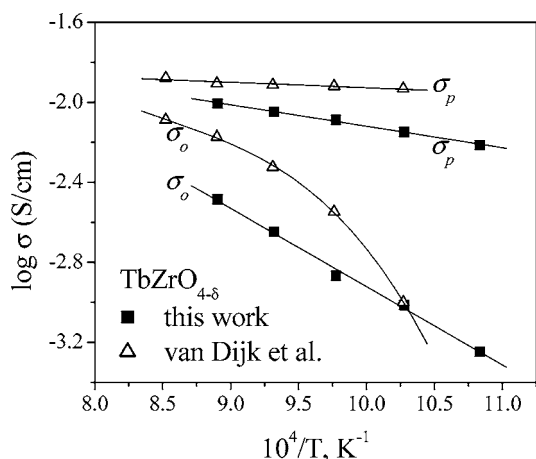
Fig. 11. Comparison of the ionic and *p*-type electronic conductivities of submicron-crystalline $TbZrO_{4-\delta}$ ceramics with literature data [4] on material with micron-scale grains. In both cases the partial conductivities are calculated from the results on transference numbers and total conductivity.

Fig. 12. Temperature dependence of the total conductivity of $TbHfO_{4-\delta}$ (A) and $TbZrO_{4-\delta}$ (B) ceramics in air, argon and 10% H_2–90% N_2 mixture, compared to the partial ionic conductivity in air.

impedance spectroscopy only distinguishes processes with differences in the relaxation frequency higher than one order of magnitude, and corresponding differences in capacitance. This might be insufficient to trace the electrical effects resulting from very high concentrations of linear defects. Alternative explanations refer to point-defect association promoted by the enlarged grain boundary, which also might lead to increasing total bulk resistivity without a separate signal in the impedance spectra, and to a space charge model ([13, 14] and references cited). If assuming a reduced boundary with excess oxygen vacancies and, consequently, a positive surface charge, space charge regions should be depleted in positive charge carriers, including both major carriers in these materials, electron holes and oxygen vacancies. This would lead to decreasing partial conductivities, as observed.

Transport Properties in Reducing Atmospheres

When the oxygen partial pressure decreases, the impedance spectra of $TbMO_{4-\delta}$ ceramics undergo significant changes associated with an increase in the bulk resistance and a greater electrode response (Figs. 8 and 9). This implies that the role of *p*-type electronic conductivity, dominant in air, decreases as expected. In the case of $TbHfO_{4-\delta}$, the values of the oxygen

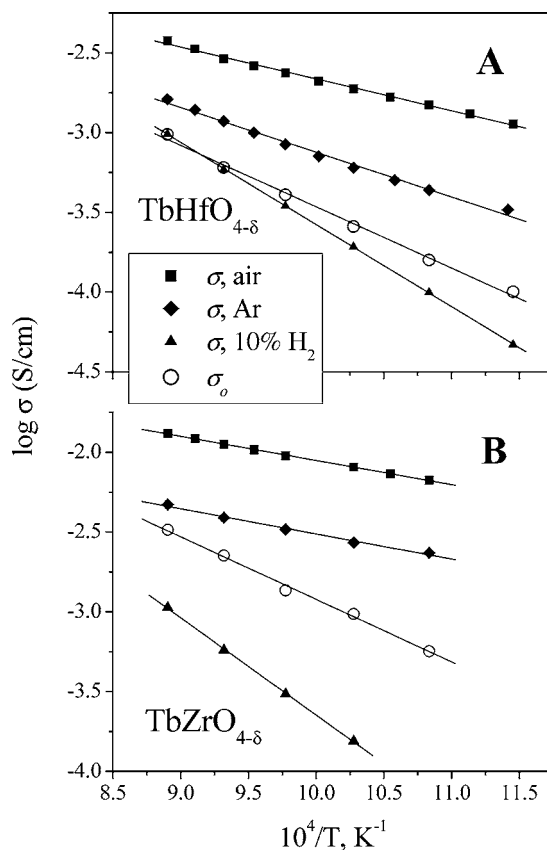ionic conductivity in oxidizing conditions are similar to the total conductivity in 10%H_2–90%N_2 mixture at 1023–1123 K (Fig. 12A). Hence, at low oxygen pressures the transport becomes almost purely ionic. At the same time, the behavior in reducing conditions, particularly the high activation energy (107 ± 1 kJ/mol), suggests a decrease in the ionic conductivity with decreasing $p(O_2)$, which may result from oxygen-vacancy association. The drop of ionic transport at low oxygen pressures is quite typical for fluorite-type materials, including acceptor-doped CeO_2. A more pronounced difference between the ionic conductivity in air and total conductivity under very reducing conditions is observed for $TbZrO_{4-\delta}$ (Fig. 12B), for which an apparent activation energy in 10%H_2–90%N_2 mixture increases up to 124 ± 2 kJ/mol. One should mention that the structural studies of $TbMO_{4-\delta}$ annealed in
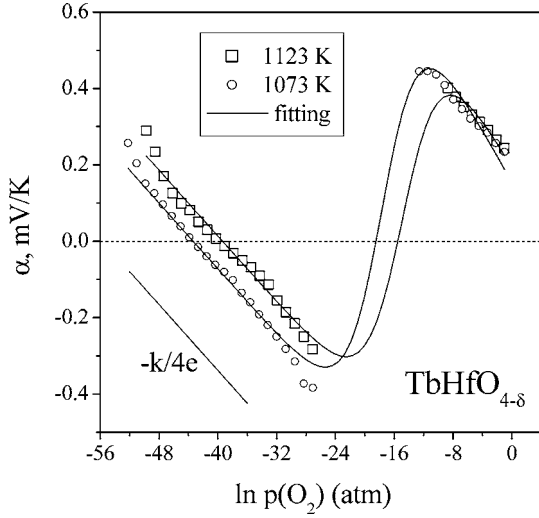
Fig. 13. Oxygen partial pressure dependence of Seebeck coefficient of TbHfO$_{4-\delta}$. Solid lines indicate the fitting results (see text).

Fig. 14. Oxygen partial pressure dependence of Seebeck coefficient of TbZrO$_{4-\delta}$. Dashed lines are for visual guidance.

hydrogen atmosphere, indicated no significant changes in their crystal lattice. Therefore, reducing oxygen chemical potential leads to vacancy ordering phenomena; if compared to partially-ordered TbHfO$_{4-\delta}$, the effect of oxygen-vacancy association on the conductivity of TbZrO$_{4-\delta}$ having a disordered lattice in air is significantly stronger. As a particular result, the assumption [4] that the ionic conductivity of terbium zirconate in oxidizing conditions is equal to its total conductivity in reducing atmospheres appears quite questionable.

The oxygen pressure dependencies of Seebeck coefficient (α) of TbHfO$_{4-\delta}$ and TbZrO$_{4-\delta}$ are presented in Figs. 13 and 14, respectively. Taking the transference numbers (Table 2) into account, the thermopower in oxidizing conditions comprises ionic (α_o) and electron-hole (α_p) contributions:

$$\alpha = t_o\alpha_o + (1 - t_o)\alpha_p \tag{1}$$

If the chemical potential of oxygen ions is essentially independent of the oxygen partial pressure, the $p(O_2)$-dependence of the ionic thermopower is determined by the equilibrium at electrodes and can be expressed as [26, 27]:

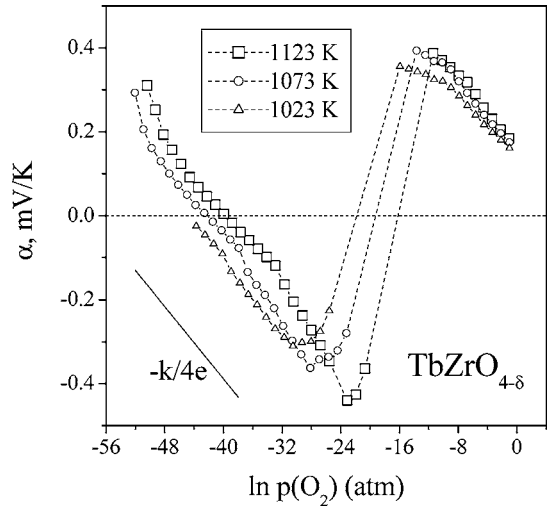$$\alpha_o = -\frac{k}{4e} \cdot \ln p(O_2) + \alpha_o^0 \tag{2}$$

where α_o^0 is the ionic Seebeck coefficient at unit oxygen activity. Such situation should take place for TbHfO$_{4-\delta}$ at temperatures above 1023 K when the ionic conductivity, essentially independent of $p(O_2)$, indicates that the oxygen-vacancy concentration is sufficiently high and, therefore, that minor variations in the oxygen nonstoichiometry should have no effect on the ion chemical potential. The electron-hole conductivity can be written as [1, 4, 26]

$$\sigma_p = F\mu_p \cdot p = \sigma_p^0 \cdot p(O_2)^{1/m} \tag{3}$$

where σ_p^0 and m are constants, μ_p and p are the hole mobility and concentration, respectively. For solid electrolytes, the values of m are typically equal to 4. As shown for TbZrO$_{4-\delta}$ [4], p-type electronic transport occurs, most likely, via a hopping between terbium ions. In this case, p-type electronic contribution to the thermopower is [28–30]:

$$\begin{aligned} \alpha_p &= \frac{k}{e} \cdot \left(\ln \frac{N - p}{p} + \frac{q}{kT} \right) \\ &= \frac{k}{e} \cdot \ln \left(\frac{N\mu_p e}{\sigma_p^0 p(O_2)^{1/m}} - 1 \right) + \frac{q}{eT} \end{aligned} \tag{4}$$

where N is the total concentration of sites participating in the conduction process, and q is the transported heat

of electron holes, which can be neglected for most semi-conductors [30]. For TbHfO$_{4-\delta}$, the ionic conductivity can be assumed $p(O_2)$-independent at least at 1073–1123 K; the ion transference numbers can be expressed as:

$$t_o = \frac{\sigma_o}{\sigma_o + \sigma_p^0 \cdot p(O_2)^{1/m}} \qquad (5)$$

Substitution of Eqs. (2)–(5) into Eq. (1) makes it possible to model $\alpha - p(O_2)$ dependencies. The fitting results, shown in Fig. 13 by solid lines, are considered as sufficiently adequate. A sharp increase in the Seebeck coefficient, found when $p(O_2)$ is lower than 10^{-22}–10^{-21} atm, may result from the influence of oxygen-vacancy association starting to affect ion chemical potential at very reduced oxygen pressures.

For TbZrO$_{4-\delta}$, the $p(O_2)$-dependence of thermopower is qualitatively similar to that of TbHfO$_{4-\delta}$, but exhibits a considerable nonlinearity and a greater slope than $(-k/4e)$ (Fig. 14). Most probably, this behavior is due to the vacancy association, which leads to the ionic conductivity at reduced $p(O_2)$ to be substantially lower with respect to oxidizing conditions (Fig. 12); the simple model for Seebeck coefficient, valid for TbHfO$_{4-\delta}$, cannot therefore be applied in this case.

Conclusions

The TbMO$_{4-\delta}$ (M = Zr, Hf) ceramics with grain size, varying in the range 50–200 nm, were prepared via mechanically-activated synthesis. XRD, SAED and IR absorption spectroscopy showed that TbZrO$_{4-\delta}$ has a disordered fluorite-type structure, whereas TbHfO$_{4-\delta}$ is partially cation-ordered. This leads to lower ionic and p-type electronic conductivities of terbium hafnate ceramics with respect to TbZrO$_{4-\delta}$. The average thermal expansion coefficients of TbMO$_{4-\delta}$, calculated from dilatometric data in air, are (11.5–12.4)×10^{-6} K^{-1} at 600–1200 K and (18.4–20.3)×10^{-6} K^{-1} at 1200–1420 K. The oxygen ion transference numbers under oxygen/air gradient vary from 0.08 to 0.26 at 873–1123 K, increasing with temperature. The activation energies for ionic and p-type electronic transport are 82–83 and 29–40 kJ/mol, respectively. The ionic conduction becomes dominant in reducing atmospheres, but tends to decrease at low $p(O_2)$, probably as a re-sult of oxygen-vacancy association, characteristic of many fluorite-type phases. If compared to data [3, 4] on TbZrO$_{4-\delta}$ ceramics with micron-scale crystallites, the enlarged grain-boundary area and presumably a high concentration of extended linear defects in the submicron-sized material leads to a slight decrease in both ionic and electron-hole conductivities.

References

1. S.A. Kramer and H.L. Tuller, *Solid State Ionics*, **82**, 15 (1995).
2. H.L. Tuller, S.A. Kramer, M.A. Spears, and U.B. Pal, *US Patent* 5509189 (1996).
3. M.P. van Dijk, K.J. de Vries, and A.J. Burggraaf, *Solid State Ionics*, **9/10**, 913 (1983).
4. M.P. van Dijk, K.J. de Vries, and A.J. Burggraaf, *Solid State Ionics*, **16**, 211 (1985).
5. B.C.H. Steele, *Solid State Ionics*, **134**, 3 (2000).
6. V.V. Kharton, A.A. Yaremchenko, E.N. Naumovich, and F.M.B. Marques, *J. Solid State Electrochem*, **4**, 243 (2000).
7. V.V. Kharton, E.N. Naumovich, and A.A. Vecher, *J. Solid State Electrochem.*, **3**, 61 (1999).
8. M. Pirzada, R.W. Grimes, L. Minervini, J.F. Maguire, and K.E. Sickafus, *Solid State Ionics*, **140**, 201 (2001).
9. B.J. Wuensch, K.W. Eberman, C. Heremans, E.M. Ku, P. Onnerud, E.M.E. Yeo, S.M. Haile, J.K. Stalik, and J.D. Jorgensen, *Solid State Ionics*, **129**, 111 (2000).
10. R.L. Withers, J.G. Thompson, and P.J. Barlow, *J. Solid State Chem.*, **94**, 89 (1991).
11. K.I. Portnoi, S.E. Salibekov, and N.I. Timofeeva, *High-Temperature Chemistry of Silicates and Oxides. Science* (Leningrad, 1972), p. 43.
12. E.I. Zoz, E.N. Fomichev, A.A. Kalashnikov, and G.G. Eliseeva, *Zh. Neorg. Khim.*, **27**, 95 (1982).
13. H.L. Tuller, *Solid State Ionics*, **131**, 143 (2000).
14. A. Tschope, *Solid State Ionics*, **139**, 267 (2001).
15. P. Yu. Butyagin and I.K. Pavlichev, *Reactivity of Solids*, **1**, 361 (1986).
16. J. Rodriguez-Carvajal, *Physica B*, **192**, 55(1993).
17. M.V. Patrakeev, E.B. Mitberg, A.A. Lakhtin, I.A. Leonidov, V.L. Kozhevnikov, V.V. Kharton, M. Avdeev, and F.M.B. Marques, *J. Solid State Chem.*, **167**, 203 (2002).
18. E.V. Tsipis, M.V. Patrakeev, V.V. Kharton, N.P. Vyshatko, and J.R. Frade, *J. Mater. Chem.*, **12**, 3738 (2002).

19. V.V. Kharton, A.P. Viskup, F.M. Figueiredo, E.N. Naumovich, A.A. Yaremchenko, and F.M.B. Marques, *Electrochim. Acta*, **46**, 2879 (2001).

20. V.V. Kharton and F.M.B. Marques, *Solid State Ionics*, **140**, 381 (2001).

21. V.V. Kharton, A.A. Yaremchenko, A.P. Viskup, G.C. Mather, E.N. Naumovich, and F.M.B. Marques, *Solid State Ionics*, **128**, 79 (2000).

22. R.D. Shannon, *Acta Cryst.*, **A32**, 751 (1976).

23. M.P. van Dijk, F.C. Mijlhoff, and A.J. Burggraaf, *J. Solid State Chem.*, **62**, 377 (1986).

24. E.L. Karyakina, E.I. Zoz, A.M. Gavrish, and N.V. Gulko, *Zh. Neorg. Khim.*, **23**, 3202 (1978).

25. V.V. Kharton, E.V. Tsipis, A.A. Yaremchenko, N.P. Vyshatko, A.L. Shaula, E.N. Naumovich, and J.R. Frade, *J. Solid State Electrochem.*, accepted for publication (2002).

26. V.N. Chebotin and M.V. Perfiliev, *Electrochemistry of Solid Electrolytes* (Khimiya, Moscow, 1978).

27. S. Yamaguchi, K. Kobayashi, K. Abe, S. Yamazaki, and Y. Iguchi, *Solid State Ionics*, **113–115**, 393 (1998).

28. G.H. Jonker, *Philips Res. Rep.*, **23**, 131 (1968).

29. P. Kofstad, Nonstoichiometry, *Diffusion and Electrical Conductivity in Binary Metal Oxides* (Wiley-Interscience, New York, 1972).

30. J. Nell, B.J. Wood, S.E. Dorris, and T.O. Mason, *J. Solid State Chem.*, **32**, 247 (1989).